

## Article

# Straw Biochar at Different Pyrolysis Temperatures Passivates Pyrite by Promoting Electron Transfer from Biochar to Pyrite

Xiaohua Shu <sup>1,2</sup> , Wei Tian <sup>1,2</sup>, Shiqing Xiong <sup>1,2</sup>, Wenlong Zhang <sup>1,2</sup> and Qian Zhang <sup>3,\*</sup>

<sup>1</sup> Guangxi Key Laboratory of Environmental Pollution Control Theory and Technology, Guilin University of Technology, Guilin 541004, China

<sup>2</sup> Guangxi Collaborative Innovation Center for Water Pollution Control and Water Safety in Karst Area, Guilin University of Technology, Guilin 541004, China

<sup>3</sup> School of Life and Environmental Science, Guilin University of Electronic Technology, Guilin 541004, China

\* Correspondence: qzhang0613@guet.edu.cn

**Abstract:** To control acid mine drainage (AMD) at source, biochar, a new green and environmentally friendly passivator has been introduced to passivate pyrite. However, the raw material and pyrolysis temperature largely determine the physical and chemical properties of biochar, the causal relationship between biochar and pyrite and the underlying mechanism are still unknown. Here, biochar materials (rice-straw biochar (RSB) and sugarcane bagasse biochar (SBB)) at different pyrolysis temperatures (300–600 °C) were utilized for the passivation of pyrite. The results of our investigations revealed that the passivation ability of RSB was superior to that of SBB. The addition of RSB with higher pyrolysis temperatures could greatly enhance the passivation efficiency of pyrite. RSB-500 (produced at a pyrolysis temperature of 500 °C) achieved the best passivation effect on pyrite. RSB can form Fe-O bonds through C=O bonding with pyrite. Moreover, the addition of RSB created a reducing environment in the mixture system because of its strong electron-donation capacity (EDC) and altered the energy-band structure of pyrite, which promoted the transfer of electrons from biochar to pyrite. On the contrary, the addition of SBB did not result in the formation of Fe-O bonds with pyrite. In addition, the EDC of SBB was also lower than that of RSB and it had almost no effect on the band structure of pyrite. Hence it did not alter the direction of the electron migration. These findings shed light on the mechanism of biochar passivation of pyrite and provide a theoretical foundation for selecting suitable biochar materials for AMD prevention at source.

**Keywords:** pyrite; biochar; AMD; surface passivation; band bending



**Citation:** Shu, X.; Tian, W.; Xiong, S.; Zhang, W.; Zhang, Q. Straw Biochar at Different Pyrolysis Temperatures Passivates Pyrite by Promoting Electron Transfer from Biochar to Pyrite. *Processes* **2022**, *10*, 2148. <https://doi.org/10.3390/pr10102148>

Academic Editors: Zenghui Diao, Guining Lu and Kaibo Huang

Received: 30 September 2022

Accepted: 19 October 2022

Published: 21 October 2022

**Publisher's Note:** MDPI stays neutral with regard to jurisdictional claims in published maps and institutional affiliations.



**Copyright:** © 2022 by the authors. Licensee MDPI, Basel, Switzerland. This article is an open access article distributed under the terms and conditions of the Creative Commons Attribution (CC BY) license (<https://creativecommons.org/licenses/by/4.0/>).

## 1. Introduction

Pyrite (FeS<sub>2</sub>) is one of the most abundant sulfide minerals in the earth's crust and is readily oxidized to form acid mine drainage (AMD), which contains many heavy metals [1,2]. In addition, other toxic elements in tailings are released with AMD, which will eventually threaten human and animal health after migration and transformation [3,4]. Therefore, the environmental problems caused by AMD need to be addressed.

Surface passivation is widely utilized as a source treatment technology because it is simple and effective for inhibiting pyrite oxidation [5–8]. A large number of passivation agents have been reported, including phosphate, humic acid, TETA, PropS-SH [9] and PSHT [10]. However, each of them has its limitations. For instance, phosphate could cause eutrophication, humic acid may not be effective in highly acidic conditions [11], TETA is toxic and costly, and low concentrations of PropS-SH can produce micro-cracks [12,13]. To overcome the above-mentioned difficulties, it is necessary to find a more suitable passivation agent which is green, safe and environmentally friendly.

As an efficient, cost-effective and environmentally friendly material, biochar is widely used in environmental remediation [14–16]. Numerous research results have indicated that the addition of biochar can prevent the migration of toxic heavy-metal elements [17] and

promote the benign growth of plants [18,19]. Wang et al. [20] added 5% rice-straw biochar and 5% alkali-modified rice-straw biochar to soil and the materials reduced available Zn contents in the soil by 28.96% and 36.86%, respectively. José Álvarez-Roge et al. [19] used biochar in sewage sludge and biochar from pruning trees as soil amendments to reduce water-soluble metals in acid mine soils and to improve plant growth. These results show that the addition of biochar materials is beneficial for reducing soil pollution. Due to the different compositions of minerals and mineral-bearing soils, their mechanisms of reaction are different. Moreover, it has been confirmed that biochar has electron-transport ability [21,22]. Zhang et al. [23] confirmed that the graphitic structure in biochar enhanced biological redox reactions by shuttling electrons. However, the effect of the electron-transport ability of biochar on the passivation of pyrite is unknown. In addition, pyrolysis temperature largely influences the surface functional groups of biochar [24,25]. The effect of the pyrolysis temperature of biochar on the passivation of pyrite is also unclear. Moreover, it is as yet unclear whether the band structure of pyrite, as a semiconductor, affects the passivation action of biochar.

In this study, rice straw and bagasse with similar structural compositions [26] were used as raw materials, these two biochar sources being widely available, cheap and clean. They are widely used in the field of soil heavy-metal pollution [14,19,20]. Biochar materials prepared from these sources at different pyrolysis temperatures were used to passivate pyrite. We conducted experiments to investigate the passivation ability and reaction mechanisms of biochar on pyrite. The experimental contents are as follows: (1) the passivation effect of the two biochars on pyrite at different pyrolysis temperatures, (2) the bonding mechanisms between the biochars and pyrite, (3) the effect of electron transfer from the biochars on the band structure of pyrite in passivation. The results revealed the passivation mechanism of biochar with respect to pyrite and that electron transfer from and the pyrolysis temperature of biochar affect the passivation of pyrite, enriching understanding of the application of biochar to semiconductor minerals.

## 2. Materials and Methods

### 2.1. Pyrite Pretreatment

The natural pyrite used in the experiment was purchased from Shangbao, Hunan Province. After grinding with a grinder, the samples were screened through a 100 mesh. Using deionized water, the samples were then washed at 1.0 g:10 mL solid–liquid run ratio 5 times, 10 min/time. The supernatants were removed and placed in 50 mL beakers and frozen in a freezer at  $-20\text{ }^{\circ}\text{C}$  for 12 h. The samples were dried for 48 h in a vacuum freeze-dryer and preserved in a dryer for later use. All chemical reagents used were of analytical grade, and the water used in the experiments was ultrapure water.

### 2.2. Preparation of Biochar Materials

For the experiments, the rice straw was obtained from Donghai, Jiangsu Province, and the bagasse from Chongzuo, Guangxi Province. The biochar materials were prepared via oxygen limitation and the temperature-control method. The raw materials bought back were first dried in an oven at  $80\text{ }^{\circ}\text{C}$ , then crushed with a grinder, screened through a 100 mesh, sealed and dried. Specifically, the straw and bagasse raw materials were put into a crucible, compacted and covered, then put into a Muffle furnace and heated to  $300\text{--}600\text{ }^{\circ}\text{C}$  for 2 h at a rate of  $10\text{ }^{\circ}\text{C}/\text{min}$ . Then, the samples were fetched out after cooling to room temperature. The biochar was crushed and screened through a 100-mesh screen for sealing and preservation. The straw and bagasse biochars were denoted RSB300-RSB600 and SBB300-SBB600, respectively.

### 2.3. Coating Processing

Pyrite samples of  $0.1 \pm 0.0005\text{ g}$  were accurately weighed and placed in 100 mL beakers. RSB and SBB prepared at different pyrolysis temperatures of 150% were added and mixed with the samples. The mixtures were called P-R300—P-R600 and P-S300—

P-S600, respectively. We added 30 mL ultrapure water to each of the above beakers, then stirred and mixed them. After 5 min of ultrasound, the pyrite samples were left for 24 h and then preserved. The dissolution experiment was carried out under ambient temperature and atmospheric pressure. Finally, the filtrates were taken out with a 0.45  $\mu\text{m}$  needle filter for the determination of total Fe (TFe),  $\text{Fe}^{2+}$  and  $\text{Fe}^{3+}$ . The original pyrite was used as the control group, named PY, and three parallel samples were set for all experiments.

#### 2.4. Testing and Analysis

The iron ion test employed the method for determining iron ions in coal-mine water (MT/T 368-2005). The ICS-1000 ion chromatograph produced by DIONEX in the United States was used for sulfate ion detection. The standard curve was made with a standard sample of pure sodium sulfate solution, and the standard deviation coefficient was  $R^2 > 0.999$ . The instrument used for Zeta potential determination was a Malvern Nano ZS90. The elemental contents of the pyrolyzed biochars were analyzed with a Series II CHNS/O.Alyzer-2400 elemental analyzer produced by the PE Company in the United States. Gas-adsorption-method specific surface area analysis (BET) was performed using the American McTristar II 3020 specific surface area analyzer. The crystal properties of pyrite were analyzed by X-ray diffraction (XRD; PANalytical B.V., Almelo, The Netherlands). The results, shown in Figure S1, indicated that the purity of the pyrite used in the experiment was high [27,28]. A Fourier transform infrared spectrometer (FTIR, IS10, Thermo Fisher Scientific, Madison, WI, USA) was used to determine the infrared spectra of the biochars. UV-vis-NIR spectra were analyzed using a PerkinElmer Lambda750 spectrometer, with the analysis of pure  $\text{BaSO}_4$  powder in the background. Electron-acceptance capacity (EAC) and electron-donation capacity (EDC) tests were performed according to Yuan [29] and Bi [30]. Electrochemical impedance spectroscopy (EIS) and corrosion current tests were conducted according to Liu [12].

#### 2.5. Preparation of Pyrite and Composite Working Electrode

F-doped  $\text{SnO}_2$ (FTO) with a resistance of 7  $\Omega$  was obtained from the NSG Company of America. The FTO was cut into small glass pieces of 1  $\times$  3  $\text{cm}^2$  and 1  $\times$  2  $\text{cm}^2$  during sample preparation. Then, 50 mg pyrite samples were weighed and evenly scattered on the conductive surface of 1  $\times$  3  $\text{cm}^2$  indium-coated FTO, compacted with 1  $\times$  2  $\text{cm}^2$  glass and fixed with copper conductive adhesive. A length of copper wire with a diameter of 1.5 mm was used to connect the glass sheet and the crocodile clip. In the same way, pyrite ore was used to prepare the control samples. Three parallel samples were taken for each test group. The CHI660 electrochemical workstation was used for electrochemical and photoelectrochemical experiments, with a three-electrode system. The saturated calomel electrode was used as the reference electrode, the 1  $\times$  1  $\text{cm}^2$  platinum electrode was used as the auxiliary electrode, and a 0.01 M HCl solution was used as the electrolyte.

### 3. Results and Discussion

#### 3.1. Ion Leaching of Pyrite

The passivation ability of RSB with respect to pyrite is superior to that of SBB. As shown in Figure 1, the inhibition effect of RSB on iron ion leaching of pyrite increased with the increase in pyrolysis temperature (Figure 1a). In particular, the leaching inhibition rate of total Fe (Total) of pyrite was 79.1% when the pyrolysis temperature of RSB was 500  $^\circ\text{C}$ . It can be concluded that RSB showed excellent inhibition ability with respect to pyrite (Table 1). On the contrary, the inhibition effect of SBB on the iron ion leaching of pyrite decreased with the increase in pyrolysis temperature (Figure 1b). The inhibition rate of SBB with respect to iron ion leaching of pyrite at different pyrolysis temperatures was generally 30%—much lower than that of RSB (Table 1). In conclusion, RSB has a better inhibition effect on iron ion leaching than SBB. In addition, the change in pyrolysis temperature for RSB had a great influence on the leaching of iron ions of pyrite, while the change in pyrolysis temperature for SBB had almost no effect on the leaching of iron ions of pyrite.

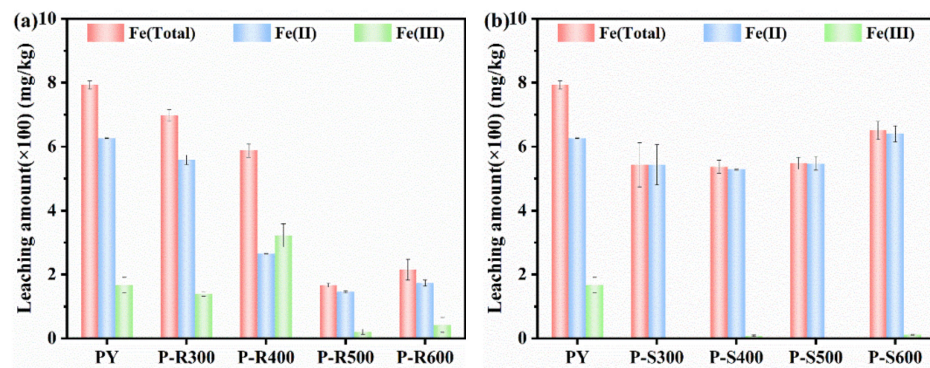


**Figure 1.** Leaching amounts of Fe(total), Fe (II) and Fe (III) of pyrite in the mixtures with the two biochars ((a) rice–straw biochar; (b) bagasse biochar) at different pyrolysis temperatures (300–600 °C).

**Table 1.** Inhibition rates of different biochars on Fe(total) leaching from pyrite.

Samples	P-R300	P-R400	P-R500	P-R600	P-S300	P-S400	P-S500	P-S600
Inhibition rate	12.1%	25.9%	79.1%	72.9%	31.5%	32.3%	30.9%	18.0%

Sulfate ion leaching was also selected as an indicator to evaluate the passivation effect of pyrite, with the results shown in Figure 2. As for the pyrite coated with RSB, the leaching amounts of sulfates decreased with the increase in pyrolysis temperature. When the pyrolysis temperature of RSB increased to 500 °C, the dissolution of sulfate ions decreased significantly (Figure 2a), while the leaching amount of sulfate ions in the P-S system increased with the increase in pyrolysis temperature (Figure 2b). It can be seen that the passivation ability of RSB is stronger than that of SBB. This result is consistent with the experimental results for iron ion leaching. Comparing Figure 2a,b, it can be concluded that different biomass sources can have great influences on the passivation effects of pyrite. In addition to biomass species, the pyrolysis temperature of biochar is also very important for the passivation effect.

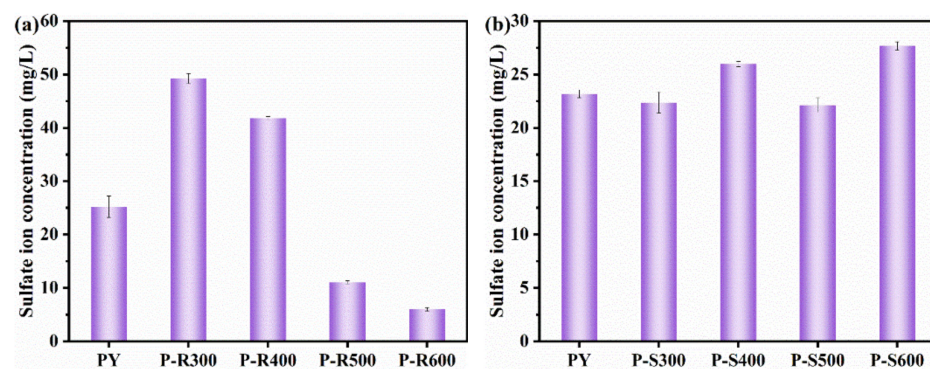


**Figure 2.** Leaching concentrations of sulfate ions of pyrite in the mixtures with the biochars ((a) rice–straw biochar; (b) bagasse biochar) at different pyrolysis temperatures (300–600 °C).

To further verify the passivation effect of biochar on pyrite, EIS tests (Figure 3) and corrosion current tests (Table S1) were carried out on the different systems. The electrochemical impedances of P-R 300–600 and P-S 300–600 were higher than that of pyrite. P-R500 showed high interfacial transfer resistance, which enhanced the passivation effect on pyrite. When the pyrolysis temperature was higher than 500 °C, the P-R system corrosion current decreased, which improved the corrosion resistance of pyrite in acidic environments. On the contrary, the corrosion current in the P-S system was higher than that in the original pyrite, which indicated that the addition of SBB is not conducive to the passivation effect of pyrite. The results are consistent with the leaching rates of iron ions and sulfate ions in the

chemical-leaching experiments, indicating that the passivation ability of RSB is superior to that of RSB.

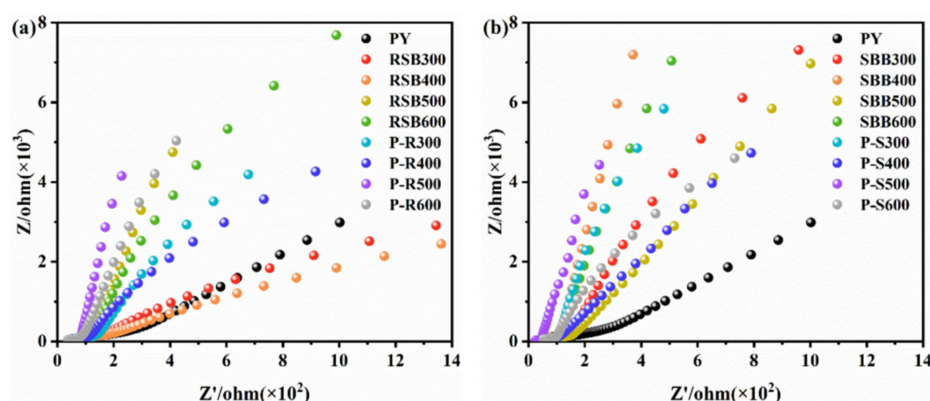


**Figure 3.** EIS test results for pyrite and biochars ((a) rice-straw biochar; (b) bagasse biochar) and the mixtures with biochars at different pyrolysis temperatures (300–600 °C).

### 3.2. The Bonding Mechanism between Pyrite and Biochar

To better understand the mechanism of the effect of biochar on pyrite, we conducted an investigation using FTIR measurements, as shown in Figure 4. RSB combined with pyrite to form Fe-O bonds, while P-S could not form Fe-O bonds. Pyrite has a characteristic peak at  $1090\text{ cm}^{-1}$ , which may be the stretching vibration of super-phase Fe-S [31]. Additionally, the P-R system retains the rich surface functional groups of the original biochar. The band at  $3407\text{ cm}^{-1}$  was attributed to O-H stretching vibration peaks in cellulose/hemicellulose. The peaks observed at  $2925\text{ cm}^{-1}$  and  $2855\text{ cm}^{-1}$  were attributed to the aliphatic C-H stretching vibration peaks, while the bands at  $1630\text{ cm}^{-1}$ ,  $1438\text{ cm}^{-1}$  and  $1399\text{ cm}^{-1}$  were attributed to the stretching vibration peaks of C=C and O=C-O on carboxyl groups, respectively. The peaks at  $1097\text{ cm}^{-1}$  and  $792\text{ cm}^{-1}$  were attributed to the stretching vibration peaks of C-O and Si-O [32–34]. In addition to the above common characteristic peaks, a new characteristic peak containing Fe was found at  $695$  and  $561\text{ cm}^{-1}$ , which corresponded to the stretching characteristic peak of the Fe-O group that is mainly attributed to the formation of iron oxide [32,35]. P-S also retained the rich surface functional groups of the original biochar. However, there was no Fe-O formation observed in the P-S compared with P-R. The above results indicated that RSB can combine with pyrite to form Fe-O to prevent the oxidation of pyrite, while SBB may have a physical shielding effect, which factors may contribute to the difference in passivation ability between RSB and SBB.

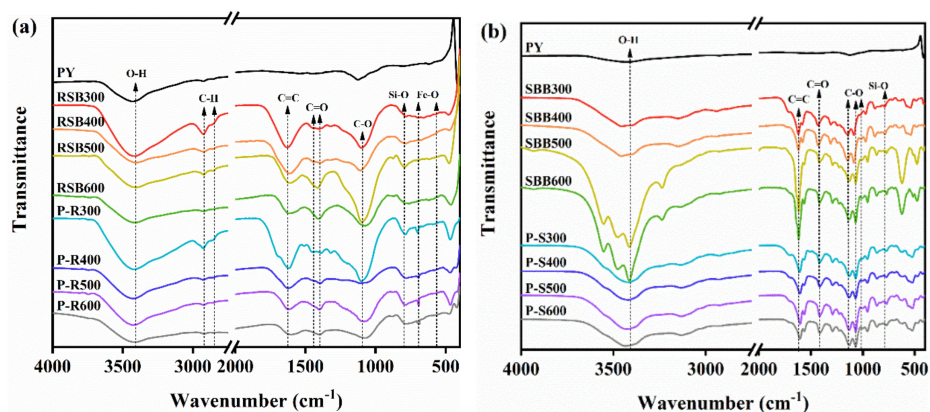


**Figure 4.** FTIR of pyrite and biochars ((a) rice-straw biochar; (b) bagasse biochar) and the mixtures with biochars at different pyrolysis temperatures (300–600 °C).

The pyrolysis temperature can affect the functional groups of biochar and then affect the bonding of biochar and pyrite. The oxygen-containing functional groups on the surface

of biochar were divided into C=O and C=C to represent the main oxidation groups and reducing groups, respectively. The selected characteristic intervals of C=O and C=C of 1800–1000  $\text{cm}^{-1}$  were quantitatively analyzed by FTIR (Figure S2). The main functional groups in the wavelength range of 1800–1000  $\text{cm}^{-1}$  were mainly C=O and C=C. According to the test results, the C=O content in RSB was greater than the C=C content, while the opposite was the case for SBB. Compared with the original biochar, the content of C=O functional groups in P-R500 decreased, while the content of C=C functional groups increased. The content of C=O functional groups in P-S500 increased, and the content of C=C functional groups decreased. In addition, with the increase in pyrolysis temperature, the H/C ratio gradually decreased (Table S2), indicating that the hydrophobicity of P-S was enhanced [36,37], which affects passivation, and RSB pyrolysis at a high temperature promoted the passivation of pyrite.

### 3.3. Effects of Electron Transfer of Biochar and the Band Structure of Pyrite on Passivation

#### 3.3.1. Effect of Electron Transfer of Biochar on Passivation

Biochar contains various redox groups and has electron-transfer ability, which may have effects on the passivation of pyrite. To explore the effect of electron transfer of biochar on passivation, we studied the electron-acceptance capacities (EACs) and electron-donation capacities (EDCs) of RSB and SBB (Figure 5). The EAC and EDC of RSB were much higher than those of SBB (Figure 5), indicating that RSB has a higher electron-transfer capability (Figure 5). The RSB had a higher EDC than SBB, indicating that RSB more readily provides a reductive environment that favors the passivation of pyrite. The above results indicated that RSB is more conducive to promoting the passivation of pyrite than SBB because RSB has a higher electron-donation capacity.

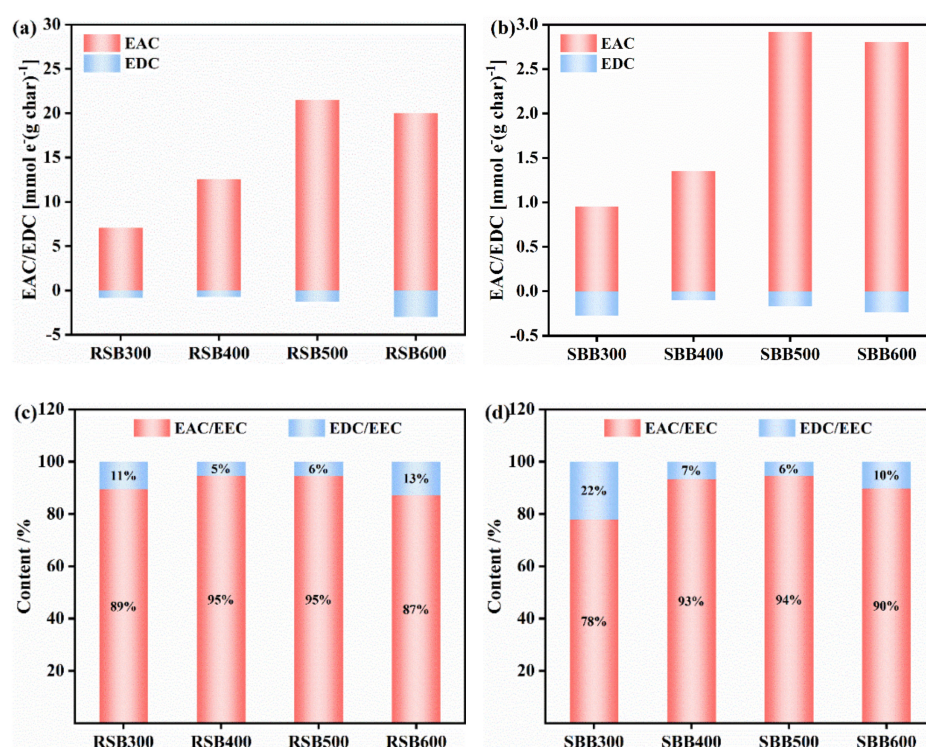


**Figure 5.** Electron-exchange capacity (EEC) of biochar at different pyrolysis temperature (300–600 °C): the EAC/EDC results for the biochars ((a) rice-straw biochar; (b) bagasse biochar) and the proportions of EEC for the biochars ((c) rice-straw biochar, (d) bagasse biochar).

Pyrolysis temperature can affect the electron-transfer capacity of biochar and then affect the passivation of pyrite. To explore the effect of pyrolysis temperature on biochar, we determined the electron-exchange capacity of biochar at different pyrolysis tempera-

tures. It can be seen that the EDC at high pyrolysis temperatures (500–600 °C) was higher than that at low pyrolysis temperatures (300–400 °C) for RSB, indicating that RSB with high-temperature pyrolysis more readily provides a reducing environment. Due to the desorption, recombination and transformation of functional groups of biochar that occurs with the increase in pyrolysis temperature [38–40], the RSB with high-temperature pyrolysis had higher C=C contents and lower C=O contents (Figure S2), indicating that biochar with a high pyrolysis temperature has a stronger reducing capacity and thus is more conducive to the passivation of pyrite.

To understand whether biochar can facilitate electron transfer to pyrite and inhibit pyrite oxidation, the redox potentials of biochar and pyrite were measured in electrochemical experiments (Table S3). The redox potential of biochar was lower than the redox potential of pyrite, indicating that the electrons in biochar can be transferred to pyrite. The redox potential of RSB was lower than that of SBB at the pyrolysis temperature of 500 °C. This may have been due to the different number of oxygenic functional groups in the raw materials. The above results indicated that a built-in internal electric field may be created which greatly facilitates electron transfer [41] between biochar and pyrite. Electrons from RSB are more easily transferred to pyrite than those of SBB, which is conducive to the inhibition of pyrite oxidation. In addition, the redox potential of P-R 300–600 becomes more negative with increasing pyrolysis temperature. The reason is that RSB, after high-temperature pyrolysis, had a higher C=C content (Figure S2). This indicated that RSB at high pyrolysis temperatures more readily donates electrons to the surface of pyrite. This result is consistent with the results for the iron ion leaching experiments and the electron-donation capacities of P-R 300–600.

### 3.3.2. Effect of the Energy-Band Structure of Pyrite on Passivation

To understand whether the band structure of pyrite can affect the electron-migration capacity in the mixed system, we investigated the band structure of pyrite before and after the passivation. The flat-band potential for each species was obtained from the intercept of a Mott–Schottky plot (Figure 6); the surface electron density could be obtained from the slope [42]. The presence of electron donors or acceptors can alter the surface electron density of a semiconductor [43], causing the energy-band bending of the semiconductor and leading to change in the flat band potential position (Table S3). The flat band potentials of P-R 500 and P-S 500 were negative to that of pyrite, indicating that RSB and SBB acted as electron donors to enhance the reduction capacities of the mixed systems. Among them, the flat band potentials of P-R 300–600 were more negative than those of P-S 300–600. This showed that RSB and SBB can negatively shift the flat band potential of pyrite, so that electrons are transferred to pyrite, and improve the reducibility of the system, which is beneficial for inhibiting the oxidation of pyrite.

High pyrolysis temperatures will promote a negative shift in the flat band potential of the P-R system, while low pyrolysis temperatures will promote a positive shift in the flat band potential of the P-R system. Compared with the original pyrite, the flat band potential moved in a positive direction in P-R 300–400, and the results for electron-transfer capacities showed that RSB300 and RSB400 acted as electron acceptors, leading to the enhancement of oxidation capacity, which was not conducive to inhibition of the oxidation of pyrite. When the pyrolysis temperature of RSB was 500–600 °C, the flat band potential moved in a negative direction, indicating that RSB500 and RSB600 acted as electron donors, leading to enhanced reduction abilities, which promoted passivation. The above results show that biochar with high pyrolysis temperatures negative the flat band potential of pyrite in mixed systems and facilitate the passivation effect.

In order to further understand the band structure of pyrite, we obtained the band gap of pyrite before and after passivation by UV–vis–NIR spectroscopy (Figure 7). Pyrite had two absorption edges in the UV range (240 nm and 390 nm), indicating that PY has a strong UV absorption capacity (Figure 7a,b). After the addition of RSB300 and RSB400, the absorption edge in the ultraviolet region disappeared, and the absorption edge appeared

at 570 nm and 580 nm in the visible region (Figure 7a). P-R 500 and P-R 600 exhibited absorption edges not only in the ultraviolet region (300 nm), but also in the visible region and even in the near-infrared region (840 nm) (Figure 7a). These results indicate that RSB500 and RSB600 extended the light absorption range of PY and enhanced the ability of PY to generate photocarriers. Conversely, the addition of SBB did not change the light absorption range of PY, so the ability to generate photocarriers was almost unchanged (Figure 7b). The band gaps of P-R and P-S are shown in Figure 7c,d. According to relevant studies in the literature, the bandgap widths (Figure 7c,d) for each material are to be calculated according to the formula  $E_g = 1240/\lambda_{Max}$ , where  $\lambda_{Max}$  is the first exciton peak [44].

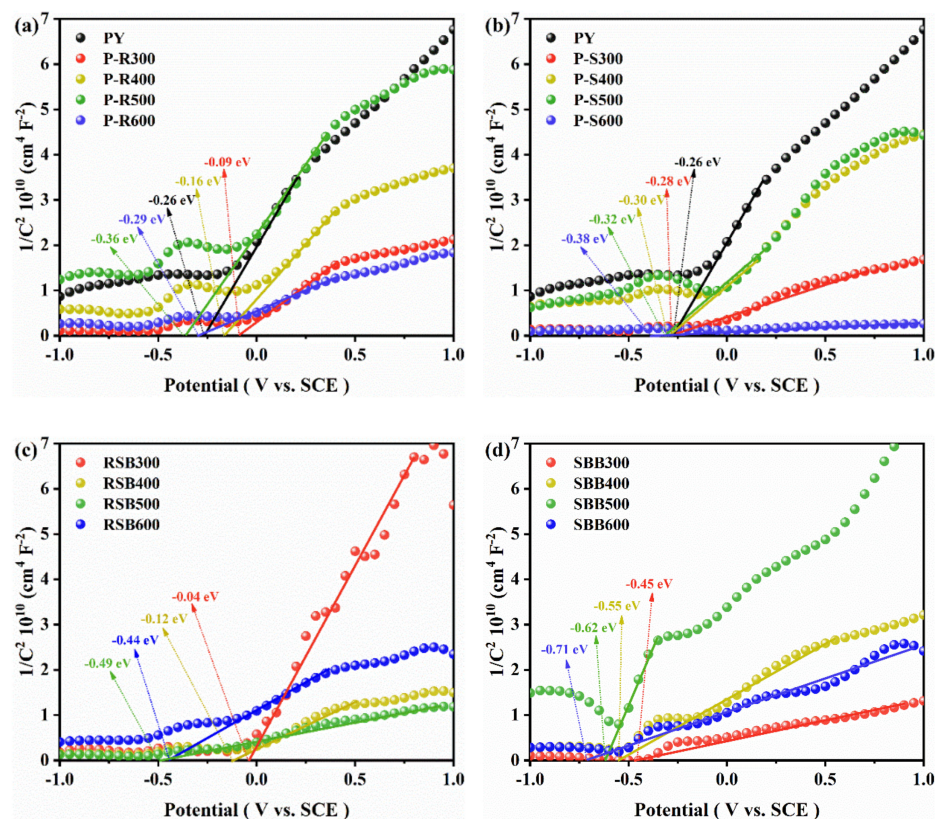


**Figure 6.** Mott–Schottky curves of substances in each system: (a) mixture of pyrite and straw biochar; (b) mixture of pyrite and bagasse biochar; (c) straw biochar; (d) bagasse biochar.

As shown in Figure S3,  $E_F$  and  $E_g$  represent flat band potentials and band gap widths, respectively. The addition of RSB500 and SBB500 made the conduction band of pyrite bend upward, which improved the reducing ability of the system and was beneficial for creating a reducing environment in the system. Compared with P-S 500, the conduction band of P-R 500 was more negative. This result indicated that P-R is more reductive and better at passivating pyrite. The forbidden band width of P-R is higher than that of P-S, so P-R can prevent pyrite from generating carriers to cause self-oxidation, which is beneficial for passivation. The above results indicated that RSB can change the band structure so that electrons from the biochar are continuously transferred to pyrite, and the P-R 300–600 systems are more reducible, which is beneficial for the passivation of pyrite.

The RSB at high pyrolysis temperatures made the conduction band of the hybrid system negative relative to the RSB at low pyrolysis temperatures. RSB at low pyrolysis temperatures made the valence band of pyrite bend downward, while RSB at high pyrolysis temperatures made the conduction band of pyrite bend upward. This showed that low-temperature RSB enhanced the oxidation of the mixed system and was detrimental to passivation, while RSB at a high pyrolysis temperature made the system reductive and facilitated passivation. These results are consistent with the results of the leaching tests.

However, the addition of SBB at different pyrolysis temperatures did not change the energy-band structure of pyrite, and its weak passivation may be due to the surface coverage of SBB, which may be only the effect of shielding.

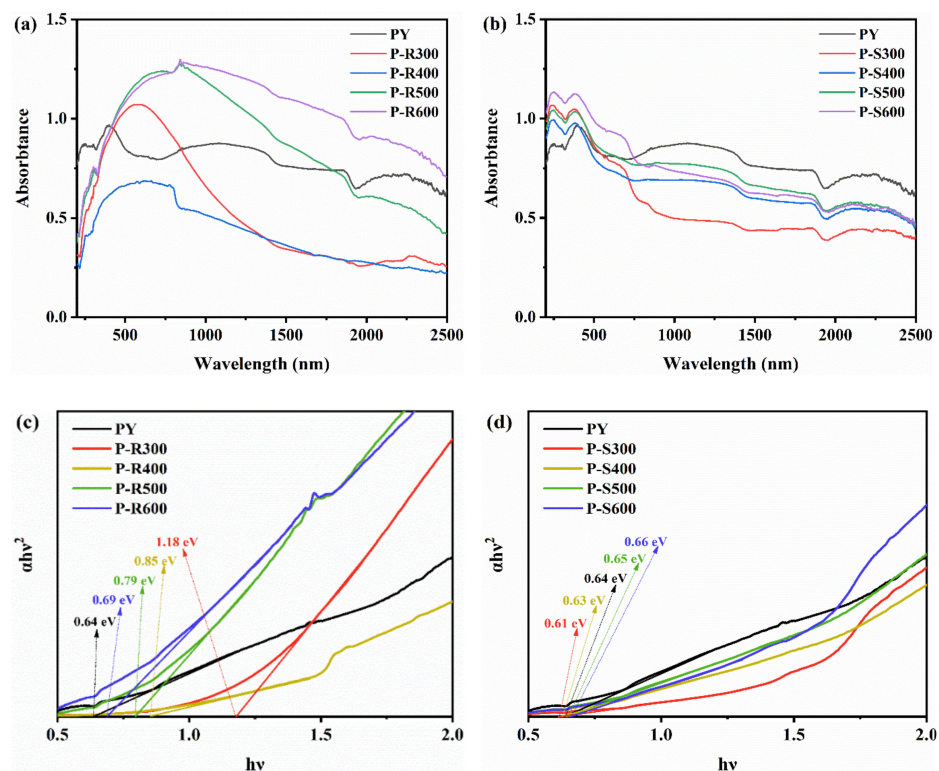


**Figure 7.** UV-vis-NIR results for pyrite and pyrite-biochar mixtures: (a) with the addition of rice-straw biochar; (b) with the addition of bagasse biochar. Plots of  $(\alpha h\nu)^2$  versus the bandgap (eV) for pyrite and pyrite-biochar mixtures: (c) with rice-straw biochar added; (d) with bagasse biochar added.

### 3.3.3. The Passivation Mechanism between Biochar and Pyrite

When Fe-O bonds were formed between the biochar and pyrite, the energy-band structure changed significantly. The formation of Fe-O bonds can influence the redox activities of biochar [45]. Fe-O bonds can promote electron transfer between biochar and pyrite [46], such that, because the redox potential of RSB was lower than that of pyrite, RSB had a higher electron-donation capacity and electrons from RSB were continuously transferred to pyrite. Due to electron transfer, biochar and pyrite generate electric fields, which cause the band structure of pyrite to bend [47]. Electrons constantly accumulate on pyrite, resulting in a change in band structure and upward bending of the conduction band. The more negative the conduction band is, the stronger the reducing ability of the hybrid system. In the P-R 500 system, the conduction band is negative to pyrite, and the bandgap is larger than that of pyrite. The change in band structure makes it more difficult for pyrite auto-oxidation to occur. The electrons accumulated in the mixed system are more susceptible to redox reactions with oxygen, which slows down the redox process of Fe ions. This is beneficial for the passivation of pyrite and inhibits the oxidation of pyrite.

## 4. Conclusions

To control acid mine drainage (AMD), biochar, a new green and environmentally friendly passivator was introduced to passivate pyrite. The passivation effect of biochar on pyrite and the underlying mechanism were demonstrated in this paper, confirming that RSB was more effective for pyrite passivation than SBB. This difference was mainly attributed to the differences in functional-group structures and electron-donation capacities

(EDCs) between the two types of biochar. RSB could create a reducing environment in the system because of its strong EDC and could alter the energy-band structure of pyrite, which promoted the transfer of electrons from biochar to pyrite. In addition, RSB, produced at higher pyrolysis temperatures, is characterized by a higher EDC and more C=C bonding as well as less C=O bonding, which facilitates the passivation of pyrite. This study has developed the surface passivation mechanism, revealed the non-negligible roles of the energy-band structure of pyrite and the electron-donation capacity of biochar in surface passivation, and has also provided a theoretical basis for selecting appropriate biochar materials to control acid mine drainage at source.

**Supplementary Materials:** The following items of supporting information can be downloaded at: <https://www.mdpi.com/article/10.3390/pr10102148/s1>, Figure S1: XRD spectra for RSB and SBB at different pyrolysis temperatures: (a) RSB; (b) SBB; Figure S2: The C=C and C=O distributions of FTIR spectra in the range of 1800–1000  $\text{cm}^{-1}$  were fitted: (a) RSB; (b) SBB; (c) P-R; (d) P-S; Figure S3: The positions of conduction bands, valence bands and Fermi energy levels for each material (vs. SCE); Table S1: Corrosion currents of probiochar and pyrite–biochar mixtures; Table S2: pH and elemental contents of biochar and pyrite–biochar mixtures; Table S3: Redox potentials and flat band potentials of pyrite and pyrite–biochar mixtures.

**Author Contributions:** Conceptualization, funding acquisition, project administration, writing—original draft, X.S.; data curation, formal analysis, writing—original draft, W.T.; writing—review and editing, S.X.; methodology, writing—original draft, W.Z.; conceptualization, supervision, writing—review and editing, Q.Z. All authors have read and agreed to the published version of the manuscript.

**Funding:** This work was financially supported by the National Natural Science Foundation of China (No. 41807392); the Natural Science Foundation of Guangxi (No. 2018GXNSFGA281001); and the Guangxi Key R&D Program Project (GuiKeAB21220049 and GuiKeAB22080071).

**Institutional Review Board Statement:** Not applicable.

**Informed Consent Statement:** Not applicable.

**Data Availability Statement:** The data presented in this study are available on request from the corresponding author.

**Conflicts of Interest:** The authors declare no conflict of interest.

## References

1. Gibert, O.; de Pablo, J.; Luis Cortina, J.; Ayora, C. Chemical characterisation of natural organic substrates for biological mitigation of acid mine drainage. *Water Res.* **2004**, *38*, 4186–4196. [[CrossRef](#)] [[PubMed](#)]
2. Zhang, S.; Wang, H.; He, X.; Guo, S.; Xia, Y.; Zhou, Y.; Liu, K.; Yang, S. Research progress, problems and prospects of mine water treatment technology and resource utilization in China. *Crit. Rev. Environ. Sci. Technol.* **2020**, *50*, 331–383. [[CrossRef](#)]
3. Liu, J.; Yin, M.; Zhang, W.; Tsang, D.C.W.; Wei, X.; Zhou, Y.; Xiao, T.; Wang, J.; Dong, X.; Sun, Y.; et al. Response of microbial communities and interactions to thallium in contaminated sediments near a pyrite mining area. *Environ. Pollut.* **2019**, *248*, 916–928. [[CrossRef](#)] [[PubMed](#)]
4. Yang, W.-J.; Ding, K.-B.; Zhang, P.; Qiu, H.; Cloquet, C.; Wen, H.-J.; Morel, J.-L.; Qiu, R.-L.; Tang, Y.-T. Cadmium stable isotope variation in a mountain area impacted by acid mine drainage. *Sci. Total Environ.* **2019**, *646*, 696–703. [[CrossRef](#)]
5. Diao, Z.; Shi, T.; Wang, S.; Huang, X.; Zhang, T.; Tang, Y.; Zhang, X.; Qiu, R. Silane-based coatings on the pyrite for remediation of acid mine drainage. *Water Res.* **2013**, *47*, 4391–4402. [[CrossRef](#)]
6. Fan, R.; Qian, G.; Short, M.D.; Schumann, R.C.; Brienne, S.; Smart, R.S.C.; Gerson, A.R. Passivation of pyrite for reduced rates of acid and metalliferous drainage using readily available mineralogic and organic carbon resources: A laboratory mine waste study. *Chemosphere* **2021**, *285*, 131330. [[CrossRef](#)]
7. Zhang, Q.; Ma, W.; Peng, Q.; Shu, X. Stabilization and Utilization of Pyrite under Light Irradiation: Discussion of Photocorrosion Resistance. *ACS Omega* **2020**, *5*, 28693–28701. [[CrossRef](#)]
8. Shu, X.; Dang, Z.; Zhang, Q.; Yi, X.; Lu, G.; Guo, C.; Yang, C. Passivation of metal-sulfide tailings by covalent coating. *Miner. Eng.* **2013**, *42*, 36–42. [[CrossRef](#)]
9. Ouyang, Y.; Liu, Y.; Zhu, R.; Ge, F.; Xu, T.; Luo, Z.; Liang, L. Pyrite oxidation inhibition by organosilane coatings for acid mine drainage control. *Miner. Eng.* **2015**, *72*, 57–64. [[CrossRef](#)]
10. Gong, B.; Li, D.; Niu, Z.; Liu, Y.; Dang, Z. Inhibition of pyrite oxidation using PropS-SH/sepiolite composite coatings for the source control of acid mine drainage. *Environ. Sci. Pollut. Res. Int.* **2021**, *28*, 11090–11105. [[CrossRef](#)]

11. Sahoo, P.K.; Kim, K.; Equeenuddin, S.M.; Powell, M.A. Current approaches for mitigating acid mine drainage. *Rev. Environ. Contam. Toxicol.* **2013**, *226*, 1–32. [[CrossRef](#)]
12. Liu, Y.; Hu, X.; Xu, Y. PropS-SH/SiO<sub>2</sub> nanocomposite coatings for pyrite oxidation inhibition to control acid mine drainage at the source. *J. Hazard. Mater.* **2017**, *338*, 313–322. [[CrossRef](#)]
13. Li, D.; Gong, B.; Liu, Y.; Dang, Z. Self-healing coatings based on PropS-SH and pH-responsive HNT-BTA nanoparticles for inhibition of pyrite oxidation to control acid mine drainage. *Chem. Eng. J.* **2021**, *415*, 128993. [[CrossRef](#)]
14. Oliveira, F.R.; Patel, A.K.; Jaisi, D.P.; Adhikari, S.; Lu, H.; Khanal, S.K. Environmental application of biochar: Current status and perspectives. *Bioresour. Technol.* **2017**, *246*, 110–122. [[CrossRef](#)]
15. Alhar, M.A.M.; Thompson, D.F.; Oliver, I.W. Mine spoil remediation via biochar addition to immobilise potentially toxic elements and promote plant growth for phytostabilisation. *J. Environ. Manag.* **2021**, *277*, 111500. [[CrossRef](#)]
16. Qin, J.; Niu, A.; Liu, Y.; Lin, C. Arsenic in leafy vegetable plants grown on mine water-contaminated soils: Uptake, human health risk and remedial effects of biochar. *J. Hazard. Mater.* **2021**, *402*, 123488. [[CrossRef](#)]
17. Penido, E.S.; Martins, G.C.; Mendes, T.B.M.; Melo, L.C.A.; do Rosário Guimarães, I.; Guilherme, L.R.G. Combining biochar and sewage sludge for immobilization of heavy metals in mining soils. *Ecotoxicol. Environ. Saf.* **2019**, *172*, 326–333. [[CrossRef](#)]
18. Puga, A.P.; Melo, L.C.A.; de Abreu, C.A.; Coscione, A.R.; Paz-Ferreiro, J. Leaching and fractionation of heavy metals in mining soils amended with biochar. *Soil Tillage Res.* **2016**, *164*, 25–33. [[CrossRef](#)]
19. Gasco, G.; Alvarez, M.L.; Paz-Ferreiro, J.; Mendez, A. Combining phytoextraction by Brassica napus and biochar amendment for the remediation of a mining soil in Riotinto (Spain). *Chemosphere* **2019**, *231*, 562–570. [[CrossRef](#)]
20. Wang, Y.; Zheng, K.; Zhan, W.; Huang, L.; Liu, Y.; Li, T.; Yang, Z.; Liao, Q.; Chen, R.; Zhang, C.; et al. Highly effective stabilization of Cd and Cu in two different soils and improvement of soil properties by multiple-modified biochar. *Ecotoxicol. Environ. Saf.* **2021**, *207*, 111294. [[CrossRef](#)]
21. Yuan, Y.; Zhou, M.; Shi, J.; Zhang, C.; Zhang, J.; Rinklebe, J.; Yin, W.; Wang, S.; Wang, X. The significant role of electron donating capacity and carbon structure of biochar to electron transfer of zero-valent iron. *Chemosphere* **2022**, *287*, 132381. [[CrossRef](#)] [[PubMed](#)]
22. Yang, Z.; Sun, T.; Subdiaga, E.; Obst, M.; Haderlein, S.B.; Maisch, M.; Kretzschmar, R.; Angenent, L.T.; Kappler, A. Aggregation-dependent electron transfer via redox-active biochar particles stimulate microbial ferrihydrite reduction. *Sci. Total Environ.* **2020**, *703*, 135515. [[CrossRef](#)] [[PubMed](#)]
23. Zhang, X.; Xia, J.; Pu, J.; Cai, C.; Tyson, G.W.; Yuan, Z.; Hu, S. Biochar-Mediated Anaerobic Oxidation of Methane. *Environ. Sci. Technol.* **2019**, *53*, 6660–6668. [[CrossRef](#)] [[PubMed](#)]
24. Zhu, M.; Kim, S.; Mao, L.; Fujitsuka, M.; Zhang, J.; Wang, X.; Majima, T. Metal-Free Photocatalyst for H<sub>2</sub> Evolution in Visible to Near-Infrared Region: Black Phosphorus/Graphitic Carbon Nitride. *J. Am. Chem. Soc.* **2017**, *139*, 13234–13242. [[CrossRef](#)]
25. Islam, T.; Li, Y.; Cheng, H. Biochars and Engineered Biochars for Water and Soil Remediation: A Review. *Sustainability* **2021**, *13*, 9932. [[CrossRef](#)]
26. Jeong, C.Y.; Dodla, S.K.; Wang, J.J. Fundamental and molecular composition characteristics of biochars produced from sugarcane and rice crop residues and by-products. *Chemosphere* **2016**, *142*, 4–13. [[CrossRef](#)]
27. Zhang, Q.; Zhou, J.; Zhang, L.; Zhong, S.; Ru, X.; Shu, X. Sulfur defect and Fe(III) (hydr)oxides on pyrite surface mediate tylosin adsorption in lake water: Effect of solution chemistry and dissolved organic matter. *Environ. Sci. Pollut. Res. Int.* **2022**. *online ahead of print.* [[CrossRef](#)]
28. Bai, X.; Ma, W.; Zhang, Q.; Zhang, L.; Zhong, S.; Shu, X. Photon-induced redox chemistry on pyrite promotes photoaging of polystyrene microplastics. *Sci. Total Environ.* **2022**, *829*, 154441. [[CrossRef](#)]
29. Yuan, T.; Yuan, Y.; Zhou, S.; Li, F.; Liu, Z.; Zhuang, L. A rapid and simple electrochemical method for evaluating the electron transfer capacities of dissolved organic matter. *J. Soils Sediments* **2011**, *11*, 467–473. [[CrossRef](#)]
30. Bi, R.; Lu, Q.; Yu, W.; Yuan, Y.; Zhou, S. Electron transfer capacity of soil dissolved organic matter and its potential impact on soil respiration. *J. Soils Sediments* **2013**, *13*, 1553–1560. [[CrossRef](#)]
31. Kong, F.; Fan, X.; Kong, A.; Zhou, Z.; Zhang, X.; Shan, Y. Covalent Phenanthroline Framework Derived FeS@Fe<sub>3</sub>C Composite Nanoparticles Embedding in N-S-Codoped Carbons as Highly Efficient Trifunctional Electrocatalysts. *Adv. Funct. Mater.* **2018**, *28*, 1803973. [[CrossRef](#)]
32. Brigante, M.; Pecini, E.; Avena, M. Magnetic mesoporous silica for water remediation: Synthesis, characterization and application as adsorbent of molecules and ions of environmental concern. *Microporous Mesoporous Mater.* **2016**, *230*, 1–10. [[CrossRef](#)]
33. Tang, J.; Huang, Y.; Gong, Y.; Lyu, H.; Wang, Q.; Ma, J. Preparation of a novel graphene oxide/Fe-Mn composite and its application for aqueous Hg(II) removal. *J. Hazard. Mater.* **2016**, *316*, 151–158. [[CrossRef](#)]
34. Wang, J.; Chen, Z.; Chen, B. Adsorption of polycyclic aromatic hydrocarbons by graphene and graphene oxide nanosheets. *Environ. Sci. Technol.* **2014**, *48*, 4817–4825. [[CrossRef](#)]
35. Guo, X.; Yang, C.; Wu, Y.; Dang, Z. The influences of pH and ionic strength on the sorption of tylosin on goethite. *Environ. Sci. Pollut. Res.* **2014**, *21*, 2572–2580. [[CrossRef](#)]
36. Niazi, N.K.; Bibi, I.; Shahid, M.; Ok, Y.S.; Burton, E.D.; Wang, H.; Shaheen, S.M.; Rinklebe, J.; Luttge, A. Arsenic removal by perilla leaf biochar in aqueous solutions and groundwater: An integrated spectroscopic and microscopic examination. *Environ. Pollut.* **2018**, *232*, 31–41. [[CrossRef](#)]

37. Tan, X.; Zhu, S.; Show, P.L.; Qi, H.; Ho, S.H. Sorption of ionized dyes on high-salinity microalgal residue derived biochar: Electron acceptor-donor and metal-organic bridging mechanisms. *J. Hazard. Mater.* **2020**, *393*, 122435. [[CrossRef](#)]
38. Kan, T.; Strezov, V.; Evans, T.J. Lignocellulosic biomass pyrolysis: A review of product properties and effects of pyrolysis parameters. *Renew. Sustain. Energy Rev.* **2016**, *57*, 1126–1140. [[CrossRef](#)]
39. Shen, D.K.; Gu, S.; Bridgwater, A.V. Corrigendum to “The thermal performance of the polysaccharides extracted from hardwood: Cellulose and hemicellulose” [Carbohydr. Polym. 82 (1) (2010) 39–34]. *Carbohydr. Polym.* **2011**, *83*, 39–45. [[CrossRef](#)]
40. Dhyani, V.; Bhaskar, T. A comprehensive review on the pyrolysis of lignocellulosic biomass. *Renew. Energy* **2018**, *129*, 695–716. [[CrossRef](#)]
41. Liu, X.; Duan, X.; Bao, T.; Hao, D.; Chen, Z.; Wei, W.; Wang, D.; Wang, S.; Ni, B.J. High-performance photocatalytic decomposition of PFOA by BiOX/TiO<sub>2</sub> heterojunctions: Self-induced inner electric fields and band alignment. *J. Hazard. Mater.* **2022**, *430*, 128195. [[CrossRef](#)]
42. Minella, M.; Maurino, V.; Minero, C.; Pelizzetti, E. Thin Film Nanocrystalline TiO<sub>2</sub> Electrodes: Dependence of Flat Band Potential on pH and Anion Adsorption. *J. Nanosci. Nanotechnol.* **2015**, *15*, 3348–3358. [[CrossRef](#)]
43. Hofmann, O.T.; Rinke, P. Band Bending Engineering at Organic/Inorganic Interfaces Using Organic Self-Assembled Monolayers. *Adv. Electron. Mater.* **2017**, *3*, 1600373. [[CrossRef](#)]
44. Zhang, C.; Fu, Z.; Hong, F.; Pang, G.; Dong, T.; Zhang, Y.; Liu, G.; Dong, X.; Wang, J. Non-metal group doped g-C<sub>3</sub>N<sub>4</sub> combining with BiF<sub>3</sub>:Yb<sup>3+</sup>, Er<sup>3+</sup> upconversion nanoparticles for photocatalysis in UV–Vis–NIR region. *Colloids Surf. A Physicochem. Eng. Asp.* **2021**, *627*, 127180. [[CrossRef](#)]
45. Xu, Z.; Xu, X.; Yu, Y.; Yao, C.; Tsang, D.C.W.; Cao, X. Evolution of redox activity of biochar during interaction with soil minerals: Effect on the electron donating and mediating capacities for Cr(VI) reduction. *J. Hazard. Mater.* **2021**, *414*, 125483. [[CrossRef](#)]
46. Hou, N.; Li, X.; Jiang, X.; Zhang, N.; Wang, R.; Li, D. The role of biochar in the photocatalytic treatment of a mixture of Cr(VI) and phenol pollutants: Biochar as a carrier for transferring and storing electrons. *Sci. Total Environ.* **2022**, *844*, 157145. [[CrossRef](#)]
47. Zhang, Z.; Yates, J.T., Jr. Band bending in semiconductors: Chemical and physical consequences at surfaces and interfaces. *Chem. Rev.* **2012**, *112*, 5520–5551. [[CrossRef](#)]